# Interdiffusion and Doping Gradients at the Buffer/Absorber Interface in Thin-Film Solar Cells

Florian Werner,*[ORCID] Finn Babbe, Jan Burkhart, Conrad Spindler, Hossam Elanzeery, and Susanne Siebentritt

Laboratory for Photovoltaics, Physics and Materials Science Research Unit, University of Luxembourg, Rue du Brill 41, L-4422 Belvaux, Luxembourg

ABSTRACT: An accurate determination of the net dopant concentration in photovoltaic absorbers is critical for understanding and optimizing solar cell performance. The complex device structure of multilayered thin-film solar cells poses challenges to determine the dopant concentration. Capacitance–voltage (C–V) measurements of $Cu(In,Ga)Se_2$ thin-film solar cells typically yield depth-dependent apparent doping profiles and are not consistent with Hall measurements of bare absorbers. We show that deep defects cannot fully explain these discrepancies. We instead find that the space charge region capacitance follows the model of a linearly graded junction in devices containing a CdS or Zn(O,S) buffer layer, indicating that elemental intermixing at the absorber/buffer interface alters the dopant concentration within the absorber. For absorbers covered with MgF_2, C–V measurements indeed agree well with Hall measurements. Photoluminescence measurements of $Cu(In,Ga)Se_2$ absorbers before and after deposition of a CdS layer provide further evidence for a significant reduction of the near-surface net dopant concentration in the presence of CdS. We thus demonstrate that interdiffusion at the absorber/buffer interface is a critical factor to consider in the correct interpretation of doping profiles obtained from C–V analysis in any multilayered solar cell and that the true bulk dopant concentration in thin-film devices might be considerably different.

KEYWORDS: doping profile, capacitance–voltage, Mott–Schottky, thin-film solar cells, diffusion
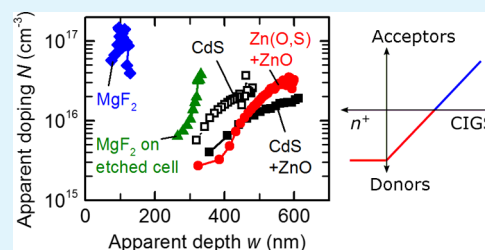
1. INTRODUCTION

Photovoltaic technologies play a crucial role for a clean and renewable generation of electricity. Solar cells based on high-quality single-crystalline semiconductors, for example, silicon or gallium arsenide, are generally most successful in terms of pure record power conversion efficiency.[1] In contrast, thin-film photovoltaic technologies emerged from the idea to reduce fabrication costs[2] and were shown to be superior in terms of energy payback time and carbon footprint.[3,4] Despite their intrinsically lower material quality, thin-film solar cells achieve remarkably high power conversion efficiencies on a laboratory scale. Recently, solar cells based on the ternary chalcopyrite semiconductor $Cu(In,Ga)Se_2$ (CIGS)[5−7] have demonstrated the highest efficiencies among all low-cost thin-film photovoltaic technologies with record efficiencies of up to 22.9%[8,9] on rigid substrates and of 20.4% using flexible substrates.[10] Efficiencies exceeding 22% have also been reported for thin-film devices based on CdTe[11] and perovskite[12] absorbers. Thin-film solar cells are complex multilayer structures.

Reliable experimental techniques to measure fundamental material properties of the semiconducting absorber layer and other constituent elements of the device are crucial to understand and optimize the performance of a solar cell. The net dopant concentration of the absorber layer, for example, significantly affects the recombination rate in the device and the width of the space charge region (SCR) at the charge-collecting p/n junction.[13] Accordingly, both open-circuit

voltage and short-circuit current density of the solar cell directly depend on the bulk dopant concentration. Correct knowledge of the doping level, thus, is a prerequisite to model or simulate thin-film solar cells or indeed any other thin-film device. The doping level can be obtained experimentally from Hall measurements or capacitance–voltage (C–V) measurements. Both methods are well established for bulk semiconductors[13−16] but are challenging to interpret in thin-film devices.[17−19] As a result, obtaining a correct description of the depth-dependent concentration of dopants in the absorber layer of a thin-film device requires particular care. In the present manuscript, we discuss CIGS devices in detail; similar effects are, however, likely to occur as well in CdTe solar cells and other thin-film devices containing heterojunctions.

On the one hand, thin-film solar cells consist of several thin layers with corresponding interfaces, as depicted on the top of Figure 1 for the example of a typical CIGS thin-film solar cell. This complex device geometry requires a complex electrical equivalent circuit[20−24] to interpret the measured capacitance and thus might have a strong impact on the extracted doping profiles. In particular, bias-dependent capacitance–voltage measurements always have to be regarded in relation to the frequency-dependent capacitance spectrum. On the other
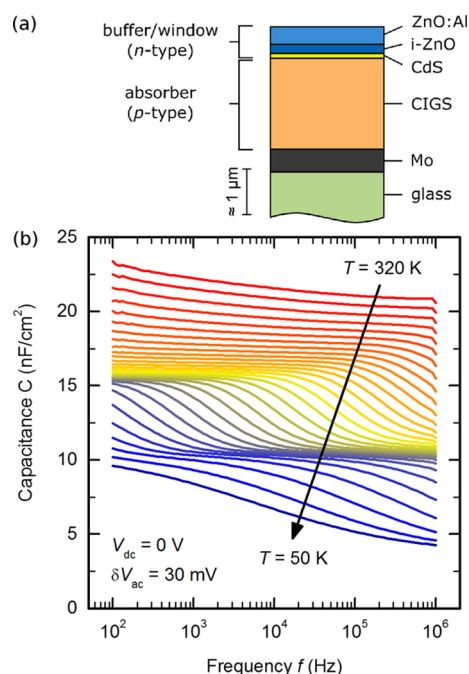
Figure 1. (a) Sketch of a typical CIGS thin-film solar cell processed on a glass substrate: a Mo back contact, a p-doped CIGS absorber layer, a CdS buffer layer, and an n-type window double layer (nonintentionally-doped "intrinsic" i-ZnO and Al-doped ZnO). The given scale is only approximate. (b) Experimental capacitance spectrum $C(f)$ of a CIGS solar cell in a measured temperature range of 320−50 K, showing a main capacitance step from 15 down to 10 nF/cm^2 in a temperature range of 250−70 K and a capacitance freeze-out at the lowest temperatures.

hand, carrier traps and recombination centers in the form of electronic defects might be present within the active CIGS absorber layer or at the buffer/absorber interface. Even at high frequencies, where capacitive contributions from such defects are typically negligible, charges stored in the defects can still affect the experimental capacitance−voltage relations if the defect level crosses the Fermi level somewhere in the absorber. This adds a bias-dependent contribution of defect states to the true concentration[25] of shallow dopants in the absorber.

In the standard approach to obtain the absorber dopant concentration from a $C−V$ measurement, the effective dopant concentration is calculated from the slope of the inverse squared capacitance C^{-2} as a function of applied bias voltage V ("Mott−Schottky plot").[15] The corresponding apparent depth is calculated from the inverse capacitance assuming a parallel plate capacitor between both edges of the SCR. Note that the SCR is typically assumed to only extend into the p-type absorber because of the (assumed) high n-type doping of the buffer/window layers. In addition to this fundamental assumption, the effect of additional layers and interfaces in the device structure is usually not taken into account. Although some authors do consider the contribution of an intrinsic interlayer to the SCR width, for example, the buffer layer in CIGS solar cells,[26−28] further effects of the n-doped side are neglected. Most importantly, however, the standard inter-pretation of $C−V$ measurements relies on the assumption of sharp and well defined "step-like" interfaces, that is, no intermixing of adjacent materials should occur within the device.

Several common features are routinely observed in the electrical characterization of CIGS thin-film solar cells.

- At least one pronounced capacitance step in thermal admittance spectroscopy with an activation energy around 100 meV, similar to that shown in Figure 1, which has been termed the N1 signature.[29] It has traditionally been interpreted as the signature of a defect level either at the interfaces[27,29] or in the bulk.[30] Recently, an increasing number of publications link this capacitance step to transport phenomena in the bulk[31,32] or transport barriers at the interfaces.[21,23,24,26,33−36]
- A "U"-shaped depth-dependent doping profile,[26,30,37−40] with a minimum dopant concentration typically in the range of a few 10^{15} cm^{-3} for moderate applied bias and significantly higher dopant concentrations toward higher forward bias ("front") and reverse bias ("back"). The increase toward forward bias is explained by minority carrier injection and parasitic resistances, whereas the increase toward reverse bias is typically attributed to the presence of deep defects.[25]

In a previous study,[19,40] we demonstrated that Hall measurements yield dopant concentrations significantly higher than that suggested by the standard interpretation of $C−V$ measurements and we argued that transport barriers or defects are most likely not sufficient to explain this discrepancy. Furthermore, a different doping in films grown directly on glass compared to those grown on Mo could also be excluded by measuring a film grown on Mo and mechanically removed from the substrate. We rather proposed that cadmium in-diffusion from the CdS buffer layer in these devices results in an increased donor concentration near the absorber/buffer interface, thus reducing the near-surface net dopant concen-tration compared to the strong p-type doping in the bulk. Such Cd in-diffusion into CIGS has indeed been directly observed,[41−45] at least within a few tens of nanometers from the interface. The copper vacancy (V_{Cu}) is expected to be a dominant acceptor in CIGS,[46−49] and substitutional Cd-on-Cu (Cd_{Cu}) is predicted to form a donor in CIGS.[50−52] Furthermore, CdS can be doped p-type by replacing Cd with Cu.[53] Accordingly, Cd diffusion from CdS to available sites on the Cu lattice in CIGS, or vice versa, could lead to a substantially reduced net doping or even type inversion near the CIGS/CdS interface.

In this contribution, we present further insight into the electrical characterization of CIGS solar cells with particular focus on doping gradients in capacitance−voltage measure-ments. In Section 3, we discuss deep defects in CIGS and explore to which extent they might be responsible for gradients in the apparent doping profile. We review the impact of doping gradients on the bias dependence of the junction capacitance in Section 4 and compare our experimental data to different junction models. We find that elemental interdiffusion between the buffer layer and absorber indeed consistently explains our electrical measurements, which we verify in Section 5 by replacing the standard CdS/ZnO buffer/window stack with alternative buffers and interfaces. We also provide a short update on our previous Hall measurements of CdS-coated absorbers grown on glass. Our electrical studies are complemented and confirmed by photoluminescence (PL) measurements of bare and CdS-covered absorbers in Section 6. Our results provide further support for interdiffusion as a

critical factor for the correct interpretation of doping profiles obtained from $C-V$ analysis.

2. EXPERIMENTAL DETAILS

We study polycrystalline CIGS thin-film absorbers, which are grown on Mo-coated soda-lime glass in a three-stage coevaporation process with varying Cu and Ga contents and incorporating a double Ga gradient. For the electrical measurements shown in this manuscript, we have exemplarily chosen absorbers with copper content of $[Cu]/([Ga] + [In]) \approx 0.98-0.99$ and average gallium content of $[Ga]/([Ga] + [In]) \approx 0.28-0.37$ as determined from energy-dispersive X-ray (EDX) measurements. Despite the Cu content close to unity estimated from EDX, these absorbers clearly show PL peaks characteristic for compensated Cu-poor material. The set of samples shown in this manuscript was chosen to minimize the impact of potential near-surface vacancy compounds in highly Cu-deficient absorbers and because these absorbers resulted in the highest solar cell efficiencies of 16–18%. We obtain comparable trends also for absorbers with different compositions, in particular for a range of Cu contents in Cu-poor samples and also for samples without Ga. Absorbers grown under Cu excess ("Cu-rich") were etched in a potassium cyanide (KCN) solution to remove Cu_xSe secondary phases developed under Cu-rich growth conditions and thus result in nominally stoichiometric absorbers. All samples contain Na, and to a certain extent K, from the glass substrate, but have not received an additional alkali postdeposition treatment.

Standard solar cells have a CdS buffer layer deposited by chemical bath deposition (CBD) for 5–6 min at 67 °C (2 mM $CdSO_4$, 50 mM thiourea, 1.5 M NH_4OH). The thickness is estimated to be 40–50 nm from typical growth rates. Alternatively, Zn(O,S) is deposited by CBD for 6 min at 75 °C (0.1 M $ZnSO_4 \cdot 7H_2O$, 0.4 M thiourea, 2 M NH_4OH, and 0.22 M H_2O_2 30%, recipe adapted from refs 54 and 55 estimated thickness 20–35 nm). On top of the buffer layer, we deposit an rf-sputtered i-ZnO/ZnO:Al double window layer and a Ni/Al front contact grid defined by electron beam evaporation through a shadow mask. Solar cells with an active area of 0.2–0.5 cm^2 are defined by mechanical scribing and achieve efficiencies above 16% at room temperature under 1 sun illumination.

For electrical measurements, samples are mounted in the dark in a closed-cycle cryostat at a base pressure below 10^{-3} mbar. The sample temperature is measured with a Si diode sensor glued onto an identical glass substrate beside the solar cells. The device conductance and capacitance are recorded with an LCR meter in a maximum frequency range of $f = 20$ Hz to 2 MHz with a controlled ac voltage amplitude of $\delta V_{ac} = 30$ mV rms, assuming a standard parallel equivalent circuit model ("G_p-C_p model"). We use the measured dc voltage across the terminals connecting the solar cell for all voltage-dependent measurements to exclude artifacts because of the internal resistance of the LCR meter. In Section 5, we use a deconvolution of the frequency-dependent impedance spectrum based on the serial electrical equivalent circuit consisting of two $R-C$ elements representing the buffer layer and main junction, respectively. This approach is detailed in ref 23.

For calibrated PL measurements, the samples are excited by the 514.5 nm line of an argon ion laser at room temperature. The emitted PL is collected by off-axis parabolic mirrors, redirected into a 303 mm spectrograph, and recorded by an InGaAs-array detector. Spectral correction is applied using a calibrated halogen lamp. The beam diameter and laser power are measured with a charge-coupled device camera and power meter, respectively, to calibrate the photon flux. The samples are cooled to a temperature of 10 K in a He-flow cryostat for low-temperature measurements. Time-resolved PL measurements are performed with a pulsed laser diode at 638 nm wavelength and 100 ps pulse width. The PL transients are recorded with a time resolution of approximately 400 ps with a near-infrared photomultiplier tube employing time-correlated single photon counting. Storage of bare absorbers in air reduces both quasi-Fermi level splitting[56] and lifetime, which can be reversed by cyanide etching. Thus, cyanide etching is necessary for bare absorbers before PL

measurements. Absorbers covered with CdS in contrast show a constant quasi-Fermi level splitting over many months.[56]

3. EFFECT OF DEEP DEFECTS ON THE DOPING PROFILE

Electronic defects within the SCR modify the capacitance–voltage relation and might thus lead to a misinterpretation of the experimental apparent doping profiles. At angular excitation frequencies well above the inverse response time of a given defect state, this defect no longer responds to the ac voltage modulation and remains in the same charge state. This causes the direct contribution of defect states to the device capacitance to vanish at high frequencies. Figure 1 shows a typical zero-bias capacitance spectrum of a Cu-poor CIGS solar cell for sample temperatures in a range of 320–50 K. First, we have to establish which features in the capacitance spectrum are actually related to deep defects. From low to high temperatures, we observe the following features.

3.1. Freeze-Out. The low-temperature capacitance step ($C \approx 10-4$ nF/cm^2) is clearly related to a freeze-out of the absorber because the capacitance drops to the geometrical capacitance $C = \varepsilon_0\varepsilon_r/d$ of the absorber layer with a thickness of $d = 2.3$ μm, assuming a relative dielectric permittivity $\varepsilon_r = 10$. It is thus not relevant for the present discussion.

3.2. Main Capacitance Step ("N1"). The main capacitance step ($C \approx 15-10$ nF/cm^2) in a temperature range of 250–70 K agrees with the N1 signature[29] commonly observed for CIGS solar cells and could in principle be related to deep defects. If this was the case, these defects could follow the ac excitation over the full experimental frequency range for $T > 250$ K and accordingly would always contribute to the capacitance near room temperature. However, on the basis of refs 23,24, and 36 we instead attribute this capacitance step to a transport barrier or interfacial/buffer layer in our devices.

3.3. Slow Defects? The slight capacitance dispersion at the highest temperatures above the main capacitance step might be caused by tail states at the band edges[57] but might also indicate the presence of slow defect states in the bulk or at the interface. "Slow" in this context refers to a capacitance step with inflection frequency well below the experimental frequency range.

According to these observations, we only expect slow defect levels that do not follow the ac excitation in a $C-V$ measurement near room temperature. Nevertheless, the charges stored in these defects at a given applied dc bias voltage will differ from the zero-bias case, unless the defect level is energetically far away from the Fermi level everywhere in the SCR. The potential distribution across the device is described by the Poisson equation, which links the potential to the total charge density including carriers in the bands, ionized dopants, and charged defects. Despite a negligible direct capacitive contribution, charged defects thus modify the band bending in the SCR and consequently also alter the SCR capacitance. This results in a "stretch-out" of the capacitance–voltage curve along the voltage axis, and the apparent doping concentration obtained from the Mott–Schottky plot increases.[15,25] For sufficiently high ac frequencies or temperatures, the only impact of defects on the doping profile thus originates from the slow variation of the dc bias voltage, which allows the defect charges to equilibrate at each measurement point on the bias voltage ramp. We indeed observe a measurable difference in the doping profiles depending on the voltage sweep rate used in the experiment (not shown

here), which suggests an influence of deep defects on the device capacitance. We thus investigate the time-dependence of the measured capacitance in response to changes in dc bias voltage to quantify the impact of deep defects on the capacitance measurement.

Because we only expect slow defect levels, we are fairly unrestricted in our choice of measurement frequency. Here, we have chosen an ac frequency of 10 kHz to avoid artifacts due to series resistance, which increase with frequency. We study the time-evolution of the SCR width due to charging or discharging of defects by the following method: the sample is kept at a forward bias of ≈700 mV, comparable to the open-circuit voltage V_{oc} under 1 sun illumination, for at least 120 s. The capacitance is continuously monitored to verify that a saturation value is reached after this time. This procedure ensures that the device is in a well-defined steady state in forward bias with all relevant trap levels above the Fermi level of the bulk majority carriers, as depicted by the top left sketch in Figure 2. The bias voltage is then set to the voltage of
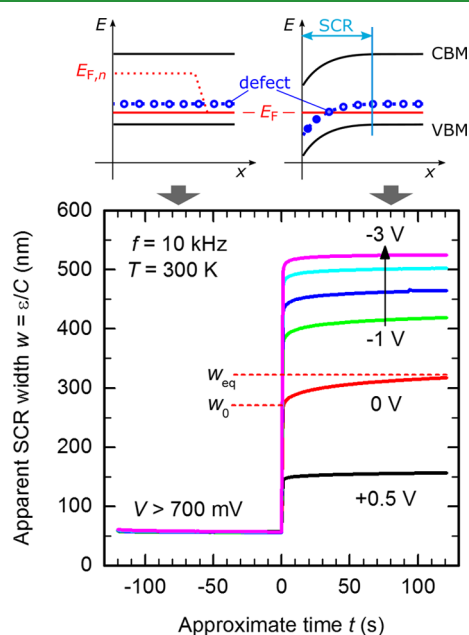

Figure 2. Top: Schematic sketch of the conduction band minimum and valence band maximum as a function of depth below the CIGS/CdS interface, with a defect level and its occupation indicated by blue circles, in forward bias (left) and in equilibrium (right). The red lines represent the majority (quasi-)Fermi level (E_F, solid line) and minority quasi-Fermi level ($E_{F,n}$, dotted line). Bottom: Evolution of the apparent SCR width $w = \varepsilon_0\varepsilon_r/C$, with $\varepsilon_r = 10$ as a function of time after keeping the device under forward bias of +700 mV immediately before applying a set bias voltage between +0.5 V and −3.0 V, as indicated in the graph. The red dashed lines exemplarily mark the initial (w_0) and final (w_{eq}) SCR width at 0 V.

interest at $t = 0$ and the capacitance is monitored for at least 120 s. Depending on the chosen bias voltage and thus band bending in the SCR, a bulk defect level might now cross the Fermi level within the SCR, as shown by the top right sketch in Figure 2. Charging or discharging of these defects will then cause a change in the SCR width with time, which manifests as a capacitance transient in the experiment. After the measurement, the device is allowed to relax at zero bias for a few minutes; then, this procedure—prebiasing at +700 mV followed by a change in bias voltage—is repeated for a

different bias voltage. Note that our admittance setup is not equipped to measure precise time-resolved capacitance transients, and the recorded transients are limited to a time resolution of approximately 1 s. This uncertainty does not influence the analysis in our study as we do not take the quantitative decay time constant into account.

Figure 2 shows a set of capacitance transients for different applied bias voltages between +0.5 V and −3 V and a sample temperature of $T = 300$ K. We plot the corresponding apparent SCR width $w = \varepsilon_0\varepsilon_r/C$ rather than the capacitance C to emphasize that the defects at the chosen frequency of 10 kHz mainly act on the potential and thus w, rather than directly on the capacitance C. Note that any intrinsic layer, for example, a depleted buffer layer, would add a constant width w_i to the SCR width, independent of the bias voltage. Throughout this paper, we assume a relative dielectric permittivity of $\varepsilon_r = 10$ for CIGS but our discussion does not depend on the exact value.

For $t < 0$, all curves in Figure 2 coincide as expected. Minor differences in capacitance correlate with variations of a few mV in the actual applied bias voltage. Note that the capacitance in forward bias shows an exponential voltage dependence because of carrier injection, and thus, small variations in bias voltage lead to a large spread in capacitance values.

When a bias voltage lower than the open-circuit voltage V_{oc} is applied at $t = 0$, the apparent SCR width increases instantly—within our measurement resolution of roughly 1 s—to an initial value w_0 and then slowly increases further to a saturation value w_{eq}. These values are indicated in Figure 2 for the example of the zero-bias transient. We interpret the initial values of the SCR width w_0 and capacitance C_0 as the ideal capacitance of the SCR in the absence of deep defects because slow defects did not yet have sufficient time to change their charge state and thus do not contribute to the capacitance at all. After some time, these defects equilibrate and additional charges localized in the defects result in an expansion of the SCR to the final width w_{eq} in steady-state conditions. Taking the initial value C_0 at each bias voltage thus allows us to construct an experimental $C–V$ curve representative of a device without any deep defects. In this interpretation, we have neglected defects with response times faster than 1 s, for which we would not be able to resolve the capacitance transient, but above a few milliseconds corresponding to an inflection frequency at the lower limit of our experimental frequency range (typically 20−100 Hz). As discussed above, we, however, do not expect such defects to be present in our devices in significant concentrations because of the small capacitance dispersion at $T = 300$ K.

It is worth pointing out that the slow defect response observed in the capacitance transients is not related to metastabilities[5] in the CIGS absorber. For a given bias voltage, we always obtain the same capacitance transient, independent of biasing or illumination history of the sample. This means that the capacitance only changes because of the slow capture and emission of charge carriers, but the nature of the defects is not altered by light soaking or by applying a bias voltage. In a different study[23] on comparable absorbers, we also did not observe any impact of the wavelength of illumination; particularly, we did not find any change of electronic or transport properties under illumination in the absence of blue light, as has been reported for certain buffer/absorber combinations earlier.[58]

4. DOPING GRADIENTS IN CAPACITANCE−VOLTAGE MEASUREMENTS

We can now compare two different sets of $C-V$ data of the same sample to investigate to which extent apparent doping gradients in CIGS devices are caused by deep defect contributions:

- The initial capacitance C_0 of the capacitance transient as described above, which we identify with the ideal SCR capacitance of a hypothetical device without deep defects and
- a conventional $C-V$ measurement at a frequency of 10 kHz, where the bias voltage is incrementally decreased from forward to reverse bias in steps of 100 mV, with a wait time of 30 s after each voltage step, which thus includes the effects of deep defects on the SCR width.

Figure 3a shows the Mott−Schottky plots, that is, inverse squared capacitance versus applied dc voltage, for the transient
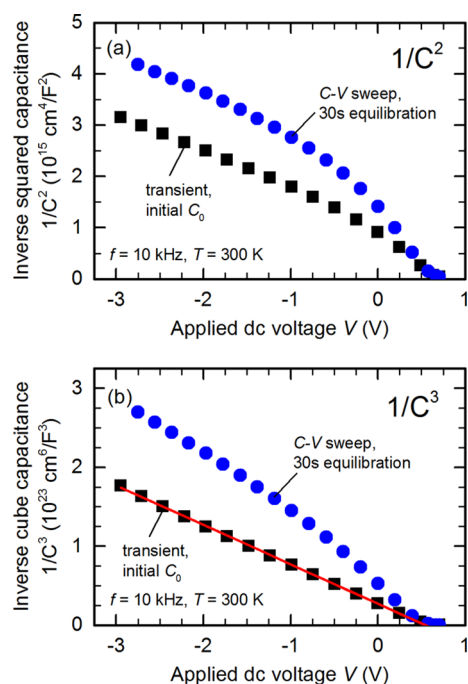

Figure 3. Voltage dependence of (a) the inverse squared capacitance $C^{-2}(V)$ and (b) the inverse cube capacitance $C^{-3}(V)$ at $T = 300$ K and $f = 10$ kHz, obtained from a standard capacitance−voltage sweep with equilibration time of 30 s (blue circles) and from the initial SCR capacitance C_0 extracted from the capacitance transients (black squares). The red solid line in part (b) is a linear fit to the data.

data (black squares) and conventional $C-V$ sweep (blue circles). The corresponding apparent doping profiles are shown in Figure 4d (solid symbols).

As expected, the Mott−Schottky plots mirror the trend seen in the capacitance transients: in the conventional $C-V$ measurement, charged slow defects increase the SCR width and lead to a clearly nonlinear Mott−Schottky plot. Note that the exact bias dependence then depends on the voltage sweep rate (not shown here). In contrast, the ideal SCR capacitance obtained from the starting value of the capacitance transients C_0 yields a much flatter doping profile. At least some part of the apparent depth dependence of typical doping profiles in CIGS devices is thus indeed related to the presence of deep defects in the SCR or at the CdS/CIGS interface. Note,
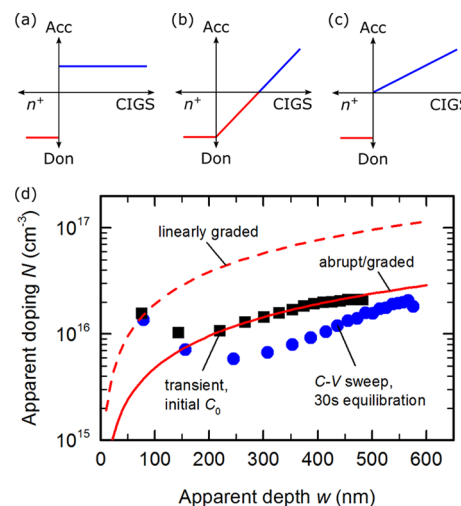

Figure 4. (a−c) Net acceptor (blue) and donor (red) concentrations near the interface between p-type CIGS bulk and n-type buffer/window layers for an (a) abrupt constant profile, (b) linearly graded profile, and (c) abrupt graded profile. For clarity, the n-type doping is drawn lower than typically assumed and any intrinsic interlayers are ignored. (d) Apparent dopant concentration N as a function of apparent depth w obtained from the Mott−Schottky plots of a standard $C-V$ sweep (blue circles) and the initial SCR capacitance of the capacitance transients (black squares). The red lines are reconstructed doping profiles for an assumed linearly graded profile [as in (b), dashed line] or abrupt graded profile [as in (c), solid line] with a slope parameter of $dC^{-3}/dV = -5 \times 10^{22}$ $(F/cm^2)^{-3}/V$.

however, that even the "ideal" capacitance does not obey a linear Mott−Schottky relation and thus indicates an inhomogeneous dopant concentration.

4.1. Fundamental Junction Models. So far, we have not addressed the implications of a potentially inhomogeneous doping profile on the analysis of capacitance−voltage measurements. Relations between various depth profiles of dopant concentration and their respective capacitance−voltage curves are discussed by van Opdorp in ref 59. On the basis of his work, we will summarize the relations relevant for the present discussion. For an arbitrary doping profile, the voltage drop V is integrated over the SCR width w according to

$$dV = -\frac{q}{\varepsilon}N(w)w \, dw \tag{1}$$

where q is the elementary unit charge, $\varepsilon = \varepsilon_0\varepsilon_r$ is the dielectric permittivity of the semiconductor, and $N(w)$ is the apparent effective doping concentration given by

$$N(w) = \left[\frac{1}{N_A(x_p)} + \frac{1}{N_D(x_n)}\right]^{-1} \tag{2}$$

where $N_A(x_p)$ and $N_D(x_n)$ are the net acceptor (donor) concentrations at the edges x_p and x_n of the SCR on the p- and n-doped side at the applied voltage V, respectively, and the total SCR width is given by $w = x_n + x_p$. The capacitance C at a given voltage is then obtained by substituting $C = \varepsilon/w$. It is generally not possible to unambiguously deduce the correct physical acceptor or donor profiles as a function of depth from a simple $C-V$ measurement alone because it requires knowledge of x_n, x_p, $N_A(x_p)$, and $N_D(x_n)$ for each bias voltage.[59] Nevertheless, information about the qualitative shape of the apparent doping profile can be obtained from

the exponent x of a linear $C^{-x}(V)$ relation, which arises from the depth-dependence of the apparent doping concentration $N(w)$ in eq 1; although the exact values of $N_{A,D}(x)$ cannot be determined, it is possible to distinguish whether the net dopant concentration changes with depth or not.

Three exemplary doping profiles relevant for the present discussion are sketched in Figure 4a–c. The constant doping model in Figure 4a represents the standard model used in most discussions, where the net dopant concentrations at the n- and p-doped sides are assumed to be uniform throughout the depth of the device with a step-like junction in-between. In this case, $N(w)$ is constant and integration of eq 1 yields

$$V_D - V = \frac{qN}{2\varepsilon}\left(\frac{\varepsilon}{C}\right)^2 \tag{3}$$

where the integration constant V_D is an offset voltage related to the built-in potential at the junction. The inverse square capacitance thus yields a straight line as a function of voltage, which explains the prominence of the Mott–Schottky plot in $C–V$ analysis. If furthermore the donor concentration in the buffer/window layers is assumed to far exceed the CIGS acceptor concentration, the effective dopant concentration in eq 2 approximately equals the CIGS net acceptor concentration. The inverse slope of the Mott–Schottky plot $C^{-2}(V)$ is then directly proportional to the approximate CIGS absorber dopant concentration.

Figure 4b represents a linearly graded doping profile, where the net donor and acceptor concentrations increase linearly with a gradient of $a = dN/dx$ with respect to distance x from the junction. Thus, $N_A(x_p) = N_D(x_n) = aw/2$ at the edges of the SCR. Integration then yields

$$V_D - V = \frac{qa}{12\varepsilon}\left(\frac{\varepsilon}{C}\right)^3 \tag{4}$$

where the denominator of the prefactor contains a factor of 3 because of the cubic dependence on capacitance and a factor of 4 from $N(w) = aw/4$ according to eq 2. The abrupt graded profile in Figure 4c represents an intermediate case between the two former extremes; here, the electronic junction coincides with the absorber/buffer interface, and only one side of the junction exhibits a gradient of the dopant concentration. For sufficiently high doping in the n-doped side, the SCR mainly extends into the linearly graded p-doped side of the junction ($w \approx x_p$), and the capacitance–voltage relation is given by

$$V_D - V = \frac{qa}{3\varepsilon}\left(\frac{\varepsilon}{C}\right)^3 \tag{5}$$

The abrupt graded profile, eq 5, differs from the linearly graded profile, eq 4, only by a factor of 4 because now $N(w) \approx N_A(x_p) \approx aw$.

For both types of graded profiles, a plot of the inverse cube capacitance $1/C^3$ versus applied voltage is thus expected to yield a straight line. A constant dopant concentration sufficiently far away from the junction, as pictured here for the highly n-doped window layer, has no effect on the $C–V$ relation if the SCR is always confined to the linearly graded section of the doping profile for the full range of bias voltages employed in the measurement. Note that linearly graded models are also good approximations for technologically more relevant exponential diffusion profiles, which can locally be approximated by a linear gradient.[59] An abrupt graded model,

on the other hand, might be applicable if the CIGS absorber always remains p-doped at the surface and the CdS buffer is unaffected by interdiffusion of Cd and Cu or always located fully within the SCR.

4.2. Comparison with Experiment. Figure 3b shows that we indeed observe a nearly perfectly linear voltage-dependence of the inverse cube capacitance obtained from the capacitance transients (ideal SCR, black squares in Figure 3b), in accordance with the predictions for a graded doping profile. From a linear fit to the data (solid red line), we deduce a slope parameter of $dC^{-3}/dV = -(5.0 \pm 0.1) \times 10^{22}$ $(F/cm^2)^{-3}/V$. This value corresponds to a doping gradient of $a = 1.9 \times 10^{14}$ cm^{-3}/nm for a linearly graded profile, eq 4, and a four times lower gradient $a = 4.8 \times 10^{13}$ cm^{-3}/nm for an abrupt/graded profile, eq 5. Reconstructed acceptor concentration profiles in the CIGS absorber based on this fit are shown by the red lines in Figure 4d as a function of the physical distance from the p/n-junction for the two different graded doping models.

For the abrupt/graded profile (Figure 4c), assuming a highly n-doped window layer, the apparent SCR width roughly coincides with the physical depth of the depletion region edge x_p within the absorber, resulting in a one-sided junction. For such a one-sided junction, the depth-dependent effective dopant concentration can be derived from the local slope of a Mott–Schottky plot $C^{-2}(V)$ around each bias voltage. As expected, the reconstructed abrupt/graded profile (solid red line in Figure 4d) thus coincides with the apparent doping profile obtained from a Mott–Schottky plot (black squares in Figure 4d). This implies that the exact junction model is not relevant for the interpretation of a $C–V$ measurement as long as the junction can be regarded as one-sided. Note that the blue circles in Figure 4d are not comparable because this doping profile includes the impact of slow defect states on the $C–V$ relation, as discussed in Section 3. All models discussed here are only valid in sufficient reverse bias, and thus, differences for small apparent depth values should also be neglected.

In contrast to the abrupt/graded case, the assumption of a one-sided junction is no longer valid for a linearly graded junction (Figure 4b). The SCR extends significantly into both the n- and p-doped side and is in fact distributed equally between both sides for an ideal linearly graded junction with the same dopant gradient in the n- and p-type sides. Accordingly, the experimental apparent doping profile underestimates the true absorber doping profile by a factor of 4 as discussed in the derivation of eq 4, a factor of 2 for the effective dopant concentration $[N_A(x_p) = N_D(x_n)$ in eq 2], and a further factor of 2 because the distance of either SCR edge from the junction is just half the total SCR width. Accordingly, the reconstructed doping profile for the linearly graded junction (dashed red line in Figure 4d) implies dopant concentrations larger than expected from the standard Mott–Schottky analysis assuming a one-sided step junction. Remarkably, the linearly graded junction model for this particular sample is consistent with a bulk dopant concentration of approximately 10^{17} cm^{-3} expected from Hall measurements[40] on comparable absorbers.

The linear voltage-dependence of the inverse cube capacitance shown in Figure 3b presents a compelling argument for a graded junction. Note that based on these $C–V$ measurements alone, we cannot differentiate between an abrupt and linearly graded junction according to Figure 4b or 4c, that is, whether the p/n junction is located at the absorber/buffer interface or within the CIGS absorber. This distinction,

however, becomes critical when trying to reconcile the low experimental doping concentrations of a few 10^{16} cm^{-3} derived from $C-V$ measurements with much higher values around 10^{17} cm^{-3} obtained by Hall measurements. Because doping profiles extracted from a Mott−Schottky plot underestimate the true physical dopant concentration for linearly graded profiles (dashed red line in Figure 4d), a buried junction within the CIGS absorber due to an (approximately) linearly graded doping profile could nicely explain the stark differences between $C-V$ and Hall measurements.

For the sample shown in Figure 4, the two different scenarios are as follows.

- Assuming a linearly graded profile, the experimental apparent dopant concentration of roughly 2×10^{16} cm^{-3} in high reverse bias (black squares in Figure 4d) corresponds to an *actual* net dopant concentration of up to 8×10^{16} cm^{-3} at the corresponding apparent depth, in good agreement with Hall results.
- For an abrupt/graded profile, the apparent doping approaches values close to 10^{17} cm^{-3} only in a depth of 2 μm because of the low gradient of $a = 4.8 \times 10^{13}$ cm^{-3}/nm. The doping gradient in this case would extend through almost the entire CIGS thin film, which has a thickness of 2−2.5 μm determined by cross section scanning electron microscopy.

On the basis of this comparison, we find that a linearly graded doping profile with a buried junction is the most natural explanation to reconcile the differences in doping level between $C-V$ and Hall measurements because $C-V$ measurements would underestimate the real doping density by a factor of up to 4. Even if we assume an abrupt/graded doping profile, where $C-V$ measurements would in principle yield the correct dopant concentration, the doping level deep within the absorber would still exceed the near-surface dopant concentration within the SCR accessible by $C-V$ measurements.

Experimentally, however, the apparent doping profile is only accessible in $C-V$ in a limited depth range, given by the location of the SCR edges for various bias voltages. Thus, we cannot determine the net dopant concentration deep within the bulk from $C-V$ and can only assume that it will level off at a dopant concentration close to that measured in Hall experiments. By the same reasoning, we would not be able to directly resolve any differently-doped, for example, intrinsic or highly p$^+$-doped, interlayers located in close proximity to the electronic junction. Note that such interlayers would, however, affect the extrapolated built-in potential,[59] which could explain why the linear fit in Figure 3b intercepts the voltage axis more than 100 meV below the 1 sun open-circuit voltage of the device. The different doping models sketched in Figure 4a−c thus have to be regarded as schematic classifications only. From the presented $C-V$ measurements, we thus conclude that a doping gradient exists in CIGS solar cells, with reduced net dopant concentration toward the absorber/buffer interface and potentially inverted n-type near-surface region within the absorber. It is, however, unlikely that a perfectly linear doping gradient throughout the full SCR forms in a real device.

5. COMPARING DIFFERENT BUFFER LAYERS

The preceding discussion indicates that doping gradients indeed exist in CIGS devices. On the basis of previous results,[40] such doping gradients could be caused by Cd in-diffusion and accordingly should be absent in devices where the CdS buffer layer is replaced by an alternative Cd-free buffer layer. We compare four different samples, which have been processed from pieces of the same substrate. All samples thus share an identical absorber but differ in the buffer/window stacks used. Their respective buffer/window stacks are as follows:

1. CBD-CdS
2. CBD-CdS with i-ZnO/ZnO:Al,
3. CBD-Zn(O,S) with i-ZnO/ZnO:Al,
4. MgF$_2$, and
5. MgF$_2$ after etching the CdS/ZnO from sample 2.

The CdS and Zn(O,S) buffer layers are deposited by CBD, whereas MgF$_2$ with a nominal thickness of 50 nm is deposited by electron beam evaporation. For sample 5, the CdS/i-ZnO/ZnO:Al stack is etched from a piece of sample 2 in diluted hydrochloric acid (HCl), and the etched surface is then covered with MgF$_2$. Note that samples with the MgF$_2$ layer did not receive any ZnO layers on top of MgF$_2$, neither did sample 1 with only a CdS layer.

In addition to electrical measurements, we performed secondary ion mass spectrometry (SIMS) on all devices. Because of the rough surface and the presence of grain boundaries, however, these SIMS measurements are not conclusive at the moment. In fact, already very small quantities below 10 ppm of electrically active donor defects, compared to approximately 4×10^{22} cm^{-3} total atoms in CIGS, are required to already fully compensate a bulk net acceptor concentration of 10^{17} cm^{-3}. It is unlikely that such small concentrations could be detected reliably by available depth- and element-specific experimental techniques such as SIMS or atom probe tomography.

The distinctly different buffer/window stacks in the five different samples might cause artifacts in the $C-V$ analysis because of their impact on the device impedance. We thus use a serial connection of two circuit elements representing the junction and buffer/window stack, respectively, each consisting of a parallel capacitance and conductance, to extract the junction capacitance at each bias voltage from the corresponding frequency-dependent impedance.[23] For devices with a CdS or Zn(O,S) buffer layer, we find that this approach is not necessary for room-temperature measurements because the conductivity of the buffer layer is high and only affects the device impedance at lower temperatures. For the less conductive MgF$_2$ layers, on the other hand, the main capacitance step is already visible at room temperature. As expected,[23] our circuit analysis results in doping profiles in agreement with standard $C-V$ measurements at low frequencies below the capacitance step. Measurements at high frequencies above the capacitance step, however, are shifted to lower absolute values of dopant concentration and higher SCR width, although they result in a qualitatively similar depth dependence. The apparent depth-dependent doping profiles at a temperature of 300 K, obtained from the circuit analysis described above, are shown in Figure 5 for all five devices. Only the reverse-bias region ($V < 0$ V) is shown for clarity because carrier injection effects start to distort the $C-V$ relation in forward bias.

5.1. Elemental Diffusion from the Buffer Layer. All samples with the CdS or Zn(O,S) buffer layer show the well-known pronounced doping gradient already observed in Section 3. If we use a thin MgF$_2$ layer (blue diamonds in Figure 5) instead of the typical buffer/window stack, we obtain
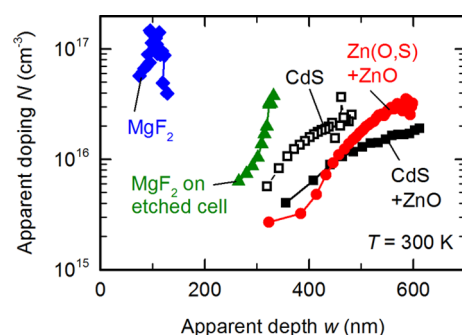
Figure 5. Apparent dopant concentration N at $T = 300$ K vs apparent depth w for different buffer/window combinations mentioned in the graph. Only reverse bias $(V < 0$ V) is shown for clarity.

a much higher apparent dopant concentration close to 10^{17} cm^{-3}, which is comparable to the (in-grain) free carrier concentration obtained by Hall measurements[40] of comparable absorbers. Accordingly, $C-V$ measurements indeed yield the correct absorber dopant concentration for this particular sample (covered with MgF$_2$) and the doping gradients observed for CdS and Zn(O,S) devices must either be real or a measurement artifact caused by the different buffer/window stacks.

If the experimental doping gradient was indeed an artifact related to the different buffer/window stack compared to a MgF$_2$ layer, it should disappear in sample 5 containing an identical MgF$_2$ layer on the etched device. In contrast, we observe a pronounced doping gradient (green triangles in Figure 5) even after replacing the buffer/window stack with MgF$_2$. The doping profile in this case is quite different from the CdS and Zn(O,S) devices but this might be in part related to the etching process; on the basis of SIMS profiles, the etched absorber appears to be 100−200 nm thinner than the initial absorber. This value is difficult to determine with any certainty and is likely insignificant compared to local thickness variations. Nevertheless, etching in HCl might indeed have removed at least some part of the original absorber surface. One might argue that the thickness of the intrinsic ZnO layer in the window stack could contribute to the apparent depth and thus explain the shift between doping profiles of samples with and without the i-ZnO layer. This is not the case in our study because we have separated the junction capacitance and any capacitive contributions of intrinsic interlayers from the frequency-dependent impedance spectrum. The impact of the i-ZnO layers on the apparent depth would anyway be small at 300 K because of their high conductivity, which is also apparent from the temperature range of the main capacitance step associated with the buffer layer in Figure 1.

5.2. Cadmium Versus Zinc. By comparing both devices with the MgF$_2$ layer, we have established that the typical dopant gradient observed in $C-V$ measurements of CIGS devices is indeed located within the absorber and not related to the presence of the buffer/window stack. This conclusion is furthermore consistent with the PL results discussed in Section 6 below. We obtain similar doping profiles for devices with CdS or Zn(O,S) buffer layers, although Zn(O,S) is nominally free of Cd. Note that we do detect small traces of Cd in absorbers covered with Zn(O,S), presumably due to the contamination of the equipment used for CBD. Migration of Zn into the absorber would likely also reduce the surface-near net dopant concentration because substitutional Zn-on-Cu

(Zn$_{Cu}$) is predicted to be a donor in CIGS as well, albeit energetically somewhat deeper than Cd$_{Cu}$.[51]

Compared to CdS, the doping gradient in the absorber with the Zn(O,S) buffer layer appears to be steeper in Figure 5, which results in a higher net dopant concentration deep within the bulk. In some cases, (not shown here) we even obtain apparent doping profiles approaching the bulk dopant concentration close to 10^{17} cm^{-3} at large reverse bias for devices containing a Zn(O,S) buffer layer. These differences between CdS and Zn(O,S) buffered devices are consistent with the literature data of the diffusion coefficients of Cd and Zn in CIGS.[60,61] The diffusion coefficient of Cd is larger than that of Zn in the relevant temperature range and we expect a deeper penetration of Cd into the CIGS absorber, whereas Zn is more confined to the surface-near region of the absorber.

Although this trend agrees with the relative magnitudes of the respective diffusion coefficients of Cd and Zn, the apparent penetration depth of several hundreds of nanometers suggested by Figure 5 is much larger than expected. Extrapolating the reported experimental diffusion coefficients[60,61] to room temperature, the penetration depth of both Cd and Zn in CIGS should not exceed a few nanometers. A few caveats have to be taken into consideration, however.

- Irregularities in the diffusion processes have been reported in these studies,[60,61] and copper vacancies and grain boundaries also enhance the diffusion process.[62−64]
- During rf-sputtering of the ZnO window layer stack, the absorber layer is exposed to elevated temperatures and the sputtering plasma. Interdiffusion might be significantly enhanced under these conditions. Already at 100 °C, for example, Cd and Zn diffusion coefficients are 3−4 orders of magnitude higher compared to their room-temperature values, which increases the penetration depth by roughly a factor of 100. At 200 °C, the penetration depth would even be 3 orders of magnitude higher compared to room temperature.
- Small quantities below 10 ppm of electrically active Cd or Zn might already be sufficient to fully compensate the bulk net acceptor concentration of 10^{17} cm^{-3}.

5.3. Complementary Electrical Measurement Techniques. Such small quantities of Cd or Zn prove difficult to detect with sufficient precision in CIGS thin-film devices, even by SIMS measurements, but their electronic effect should be readily detectable in Hall measurements. Nevertheless, we did not observe any effect of CdS deposition on the in-grain carrier concentration in our earlier Hall experiments.[19,40] A standard Hall measurement probes the full cross section of the sample and is thus less sensitive to the near-surface doping than $C-V$ measurements. Accordingly, the initial interdiffusion restricted to a near-surface layer might have gone undetected because of the high conductivity of the unaffected part of the highly-doped CIGS layer. We expect a more drastic change of the doping profile after some time because the Cd diffusion appears to proceed noticeably even at room temperature.[40] We have thus attempted to repeat Hall measurement of the same sample after storage for 18 months in vacuum. The resolution of these measurements is insufficient to obtain reliable results for the majority carrier concentration and mobility, in large part because of a strong increase of the sheet resistance over time. The absorber layer initially had an average resistivity of approximately 35 Ω cm at $T = 270$ K, which increased to 60 Ω

cm after CdS deposition mainly due to increased band bending at the grain boundaries.[40] After 18 months of storage in vacuum, we measure a resistivity of 165 Ω cm, which clearly indicates that the transport properties of the CdS-coated absorber have changed with time even when stored at room temperature. Although part of the increase in resistivity might again be due to changes of the grain boundary potential, these results would also be consistent with a substantial decrease of net dopant concentration in parts of the absorber layer.

In the literature, cross sections of CIGS devices have been studied by spreading resistance and electron beam induced current (EBIC) techniques, see, for example, refs 65 and 66 to map the majority carrier concentration and current collection by the SCR, respectively. This allows in principle to reconstruct the laterally and depth-resolved local dopant concentration within the absorber. Spreading resistance maps recorded at flat band conditions in ref 65 revealed a highly resistive near-surface layer, which has been attributed to type-inversion because of Cd diffusion into the absorber. This effect was far more pronounced in Cu-depleted samples, indicating that Cd diffusion indeed preferentially proceeds via Cu vacancies. It is worth pointing out, however, that this study only found a low doping efficiency of Cd in CIGS because the surface-near Cd-doped n-type layer was much lower doped than the p-type absorber. Such a low doping efficiency, however, only affects the formation of an inverted n-doped layer, whereas Cd is apparently still able to efficiently compensate the p-type absorber doping, leading to a doping gradient. This suggests that the donor state associated with the Cd_{Cu} defect energetically lies fairly deep below the conduction band. Recent EBIC measurements[67] revealed that the magnitude and fluctuations of the SCR width within the p-type absorber strongly depend on the buffer and window layers used in the device stack, which also supports interdiffusion processes between these layers and the CIGS absorber to have a noticeable impact on the electronic bulk properties. Both spreading resistance and EBIC measurements show that the net dopant concentration in the absorber might differ significantly between different grains.[65−67] This effect cannot be resolved by macroscopic $C-V$ measurements, which average over many grains but might contribute to differences between (perpendicular) $C-V$ and (lateral) Hall measurements. Accordingly, although all of these results from different electrical measurements support a reduced net doping concentration near the p/n-junction because of interdiffusion processes between the buffer or window layer and absorber, the actual bulk doping concentration deep within the absorber cannot be determined reliably by $C-V$ measurements and furthermore might vary significantly with lateral position.

6. ROLE OF CADMIUM STUDIED BY PL

PL experiments on bare and CdS-coated absorbers provide further evidence for fast Cd in-diffusion into the surface-near regions of the CIGS absorber. CIGS absorbers with different copper contents show distinct differences in their respective low-temperature PL spectra because of the different compensation ratios N_D/N_A, that is, the ratio of compensating donor concentration to the total acceptor concentration.[68,69] A high compensation ratio leads to local fluctuations of the electrostatic potential, thus broadening the PL emission peaks and resulting in a stronger shift of the PL peaks with increasing excitation intensity. Because of their high concentration of native point defects, Cu-poor absorbers with [Cu]/([In] +

[Ga]) < 1 usually exhibit only a single broad, asymmetric PL emission peak. In contrast, individual donor−acceptor-pair and excitonic transitions can be resolved for nearly stoichiometric absorbers grown under Cu excess ("Cu-rich").[68,69] Figure 6
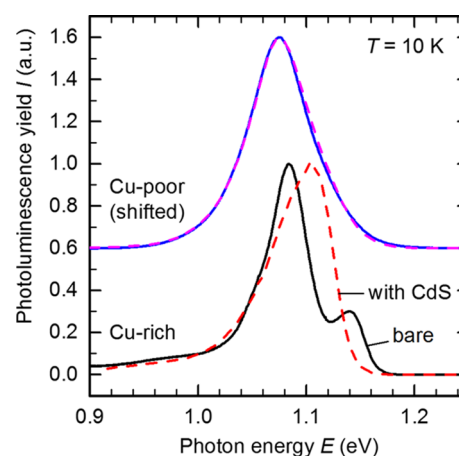

Figure 6. PL spectra recorded at T = 10 K for Cu-rich and Cu-poor (data shifted vertically by +0.6 for clarity) absorbers before (solid lines) and directly after (dashed lines) CBD of a CdS layer.

shows the low-temperature (T = 10 K) PL spectra of bare Cu-poor and Cu-rich CIGS absorbers before (solid lines) and directly after (dashed lines) depositing a standard CdS layer by CBD. The Cu-rich absorber had been etched in a KCN solution prior to the PL experiment to remove Cu_xSe secondary phases developed under Cu-rich growth conditions.

For the bare *Cu-rich* absorber, we initially clearly resolve several individual transitions, which are broadened into a single asymmetric peak after CdS deposition. Such an asymmetric broadening is similarly attributed to an increased compensation ratio within the absorber, that is, an increase in donor concentration or a decrease in acceptor concentration upon CdS deposition. In addition, the main peak at 1.08 eV shifts by 3 meV/decade with increasing excitation intensity for the bare Cu-rich absorber, indicating a low degree of compensation. After CdS deposition, this peak shifts by more than 12 meV/decade, typically related to a strong electrostatic fluctuation caused by compensating donors.[68] It should be noted that these measurements are performed at low temperatures, where the free carrier mobility is low.[19,40,70] This means that the PL emission stems predominantly from the region where absorption of the excitation laser takes place, that is, from the first ∼100 nm near the surface. Thus, by adding a CdS layer onto a Cu-rich absorber, we observe that its compensation is increased, in agreement with Cd in-diffusion, which results in a lower doping level near the surface. The bare *Cu-poor* absorber only shows a single broad PL peak, which is only slightly broadened upon CdS deposition. This can be attributed to the already high compensation of the bare absorber in the Cu-poor case, and any further increase of the compensation ratio would not strongly alter the peak shape any further.

Further evidence for a reduced doping level after CdS deposition comes from time-resolved PL measurements on polycrystalline CIGS absorbers at room temperature. Figure 7a shows exemplary time-resolved PL measurements of two different sets of bare and CdS-coated Cu-poor absorbers, which demonstrate that the experimental PL decay curves are
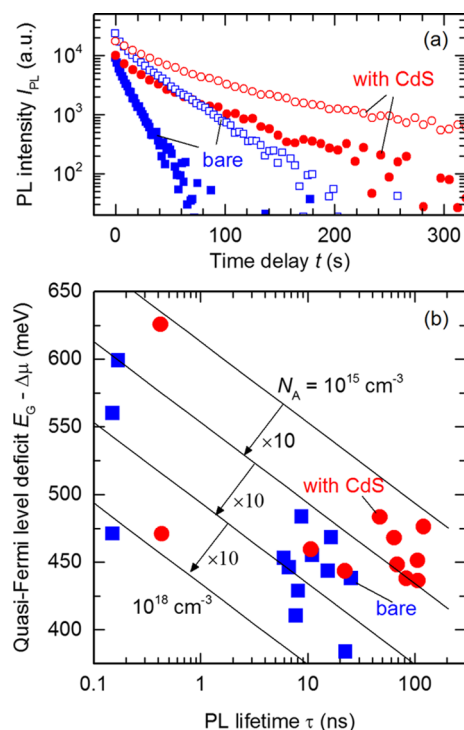
Figure 7. (a) Time-resolved PL measurements of two different Cu-poor absorbers (open and closed symbols, respectively): bare absorber (blue) and with CdS (red). (b) Quasi-Fermi level splitting deficit $E_G - \Delta\mu$ as a function of PL lifetime τ for bare (blue squares) and CdS-covered (red circles) CIGS absorbers. The solid lines represent calculated trends according to eq 7, where the dopant concentration N_A is each time increased by 1 order of magnitude from approximately 10^{15} cm^{-3} (top) to 10^{18} cm^{-3} (bottom).

not monoexponential. We fit the experimental data with the sum of three exponential decays $I_{PL}(t) = \sum_i A_i \exp(t/\tau_i)$ and estimate a mean PL lifetime τ as weighted average $\tau = \sum_i A_i \tau_i / \sum_i A_i$. These results are similar to a single exponential fit in an intermediate time range but remove the ambiguity of having to manually define a fitting range.

We compare the quasi-Fermi level splitting $\Delta\mu$ and PL lifetime τ before and after CdS deposition. Because $\Delta\mu$ is proportional to the band gap E_G of the absorber, we rather discuss the quasi-Fermi level splitting *deficit* $E_G - \Delta\mu$, that is, the difference between band gap and quasi-Fermi level splitting. Besides the band gap, the quasi-Fermi level splitting also depends on the excitation, which is kept constant in all measurements, on the amount of nonradiative recombination described by the reduced PL lifetime τ, and on the doping density N_A.[71] We use a simple model to relate lifetime τ and quasi-Fermi level splitting $\Delta\mu$

$$\Delta\mu = kT \ln\left(\frac{N_A \Delta n}{n_i^2}\right) = kT \ln\left[\frac{N_A \alpha j_{ph} \tau}{N_C N_V \exp\left(-\frac{E_G}{kT}\right)}\right] \quad (6)$$

where k is Boltzmann constant, T is temperature, N_A is net dopant concentration, Δn is the excess carrier concentration, n_i is the intrinsic carrier concentration, α is the inverse absorption length, j_{ph} is the photon flux of the excitation, N_C and N_V are the effective density of states of the conduction and valence bands, respectively, and E_G is the band gap. Equation 6 is only valid in low excitation, which was ensured by the experimental

conditions. We obtain an expression for the quasi-Fermi level splitting deficit by rearranging eq 6

$$E_G - \Delta\mu = kT \ln\left[\frac{C}{\tau N_A}\right] \quad (7)$$

where the constant $C = (N_C N_V)/(\alpha j_{ph})$ in the enumerator has the same value for all samples in our study. This deficit is thus higher for increased nonradiative recombination, that is, for lower lifetime, but also increases for lower dopant concentrations.

Figure 7 shows experimental values of the quasi-Fermi level splitting deficit $E_G - \Delta\mu$ as a function of PL lifetime τ for bare (blue squares) and CdS-covered (red circles) absorbers. In both cases, the low lifetimes below 1 ns are observed for Cu-rich absorbers and the higher ones for Cu-poor CIGS. The quasi-Fermi level splitting $\Delta\mu$ of freshly etched or freshly prepared absorbers is identical within error to the one on absorbers covered with CdS.[72] In contrast to the quasi-Fermi level splitting, which essentially remained unchanged, the carrier lifetime determined by time-resolved PL measurements at room temperature changes considerably between freshly etched and CdS-covered absorbers. Various bare absorbers measured directly after etching show average lifetimes between 5 and 20 ns (Cu-poor) and around 0.1 ns (Cu-rich). PL lifetimes of the same samples with a CdS buffer vary between 10 and 100 ns (Cu-poor) or around 0.5 ns (Cu-rich).

A similar quasi-Fermi level splitting within the same absorber, despite the pronounced differences in lifetime, is best described by a change in dopant concentration. For the constant C in eq 7, we estimate a value of $C \approx 1.6 \times 10^{16}$ s/cm^3 for our samples, assuming 1 sun illumination, $N_C = 7 \times 10^{17}$ cm^{-3} and $N_V = 1.5 \times 10^{19}$ cm^{-3} corresponding to effective electron and hole masses of 0.09 and 1.0, respectively, and assuming that α is given by the inverse absorber thickness at room temperature. Note that the factor α in eqs 6 and 7 converts the incident photon area density to a volume density of photoexcited carriers. Because excess carriers initially generated near the absorber surface redistribute throughout the absorber in a quasi-static PL measurement, the appropriate value of α will be smaller than the absorption coefficient in CIGS. Solid lines in Figure 7 show calculated relations between quasi-Fermi level splitting deficit and lifetime calculated from eq 7 for different dopant concentrations. From top to bottom, the dopant concentration increases from approximately $N_A = 10^{15}$ to 10^{18} cm^{-3} by 1 order of magnitude between two calculations. As can be seen in Figure 7, most of the measurements on CdS-covered absorbers (red circles) can be described by doping levels around approximately 10^{16} cm^{-3}, about 1 order of magnitude lower than $N_A \approx 10^{17}$ cm^{-3} of bare absorbers (blue squares). The exact numbers depend on the assumptions made for α, N_C, and N_V, but relative trends do not depend on these assumptions. Thus, also the time-dependent PL measurements indicate a reduced doping of the front part of the absorber, which is accessible by PL, after the CdS deposition.

Our PL results thus support the model that substantial Cd in-diffusion could proceed quickly even at moderate temperatures of 70 °C or below during CdS deposition. Note that, in addition, Cu from the absorber might diffuse into the CdS layer, thus representing an intermixing of the CdS and CIGS layers at the interface.

7. DISCUSSION

The electrical characterization of thin-film solar cells by means of capacitance–voltage ($C-V$) measurements was addressed with particular focus on the dopant concentration of the absorber layer in CIGS solar cells. We specifically focused on discrepancies between $C-V$ and Hall measurements and on the correct interpretation of depth-dependent doping profiles determined by $C-V$ profiling, which show an increasing apparent net acceptor concentration with depth.

The time-dependence of the device capacitance recorded at different bias voltages showed a clear saturation behavior, indicating a noticeable effect of "slow" defect states with characteristic time constants of seconds or even minutes, and thus well below the frequency range accessible in thermal admittance spectroscopy. Although these defect states do influence the apparent doping profile, they mainly act to expand the SCR width and only have a minor effect on the doping gradient. The ideal deep-defect-free SCR capacitance estimated from the experimental capacitance transients accordingly still indicates a reduced net dopant concentration near the buffer/absorber interface. A depth-dependent doping profile is typically analyzed by calculating the local slope of a Mott–Schottky plot $C^{-2}(V)$. Although this produces the correct *apparent* doping profile as a function of *apparent* depth for an arbitrary device, it does not provide any further insight into the physical origin of such a profile. Here, it is useful to additionally consider different exponents x for $C^{-x}(V)$; the inverse squared capacitance $C^{-2}(V)$ yields a straight line as function of voltage for constant dopant concentrations, whereas the inverse cube capacitance $C^{-3}(V)$ yields a straight line for linearly graded doping profiles. We showed that the ideal deep-defect-free SCR capacitance estimated from the capacitance transients indeed perfectly follows the model of a linearly graded junction for our devices. On the basis of this observation, the true dopant concentration deep within the absorber bulk might indeed be severely underestimated by conventional $C-V$ analysis, both due to the correction factor in the model for a nonabrupt junction and due to a reduced net doping within the SCR.

Our model of a modified dopant concentration in devices including a buffer layer was verified by comparing different buffer layers deposited onto the same absorber. Although the typical "U"-shaped apparent doping profile was found for both CdS and Zn(O,S) buffer layers with the i-ZnO/ZnO:Al window layer, this effect was completely absent when using a thin MgF_2 layer instead. The apparent dopant concentration close to 10^{17} cm^{-3} for the MgF_2-covered absorber in fact agrees with free carrier concentrations previously obtained by Hall measurements on similar absorbers. We showed that this result is not an artifact because of parasitic effects of the buffer/ window layers on the capacitance measurement by etching off the CdS/ZnO buffer/window stack and subsequently covering the etched absorber with MgF_2. We still found a pronounced doping gradient in this sample, indicating that the deposition of the initial buffer/window stack prior to the etching led to a physical change of the absorber near the surface. We expect these changes to be related to Cd or Zn diffusion from the buffer layer into the absorber, which could increase the donor concentration (Cd_{Cu}, Zn_{Cu}) and reduce the acceptor concentration (V_{Cu}) in the CIGS absorber close to the interface. This diffusion proceeds even at room temperature and the net dopant concentration of a given sample will change over time.[40] Although we consider Cd and Zn incorporation to most probably occur via vacancies in the copper lattice, other mechanisms or incorporation on other lattice sites might equally play a role and might also explain differences between different buffer layer materials.

Our results from electrical characterization were shown to be consistent with PL studies of bare absorbers and absorbers covered with CdS. Deposition of CdS increases potential fluctuations in the absorber, in particular for CIGS absorbers grown under Cu excess, which initially are virtually free of potential fluctuations. Furthermore, the relation between quasi-Fermi level splitting and PL lifetime could only be modeled by a significantly reduced dopant concentration in absorbers covered with CdS compared to bare absorbers. The PL experiments are thus in good agreement with a substantial reduction in near-surface net dopant concentration caused by increased donor/acceptor compensation upon deposition of a CdS layer.

8. CONCLUSIONS

Our results demonstrate that interdiffusion at the absorber/ buffer interface of CIGS thin-film solar cells is a critical factor to consider in the correct interpretation of doping profiles obtained from $C-V$ analysis. The net dopant concentration near the absorber/buffer interface is significantly reduced in devices with Cd- or Zn-containing buffer layer compared to bare absorbers. On the one hand, the true bulk dopant concentration deep within the absorber might thus be far larger than previously expected. On the other hand, the choice of the buffer layer material could be of particular importance by determining the deep and shallow defect concentrations within the SCR, which is the most crucial component of a typical solar cell.

■ AUTHOR INFORMATION

Corresponding Author
*E-mail: florian.werner@uni.lu.

ORCID ⓘ
Florian Werner: 0000-0001-6901-8901

Notes
The authors declare no competing financial interest.

■ REFERENCES

(1) Green, M. A.; Hishikawa, Y.; Dunlop, E. D.; Levi, D. H.; Hohl-Ebinger, J.; Ho-Baillie, A. W. Y. Solar Cell Efficiency Tables (Version 51). *Prog. Photovoltaics Res. Appl.* **2018**, *26*, 3−12.
(2) Zweibel, K. Thin Films: Past, Present, Future. *Prog. Photovoltaics Res. Appl.* **1995**, *3*, 279−293.
(3) Peng, J.; Lu, L.; Yang, H. Review on Life Cycle Assessment of Energy Payback and Greenhouse Gas Emission of Solar Photovoltaic Systems. *Renew. Sustain. Energy Rev.* **2013**, *19*, 255−274.

(4) de Wild-Scholten, M. J. Energy Payback Time and Carbon Footprint of Commercial Photovoltaic Systems. *Sol. Energy Mater. Sol. Cells* **2013**, *119*, 296−305.

(5) Rau, U.; Schock, H. W. Electronic properties of Cu(In,Ga)Se 2 heterojunction solar cells-recent achievements, current understanding, and future challenges. *Appl. Phys. A* **1999**, *69*, 131−147.

(6) Scheer, R.; Schock, H. W. *Chalcogenide Photovoltaics: Physics, Technologies, and Thin Film Devices*; Wiley-VCH: Weinheim, Germany, 2011.

(7) Shafarman, W. N.; Siebentritt, S.; Stolt, L. *Cu(In,Ga)Se₂ Solar Cells*, 2nd ed.; Wiley and Sons: Chichester, U.K., 2011.

(8) Solar Frontier. *Solar Frontier Achieves World Record Thin-Film Solar Cell Efficiency of 22.9%.* Press Release, 2017.

(9) Jackson, P.; Wuerz, R.; Hariskos, D.; Lotter, E.; Witte, W.; Powalla, M. Effects of Heavy Alkali Elements in Cu(In,Ga)Se₂ Solar Cells With Efficiencies up to 22.6%. *Phys. Status Solidi RRL* **2016**, *10*, 583−586.

(10) Chirilă, A.; Reinhard, P.; Pianezzi, F.; Bloesch, P.; Uhl, A. R.; Fella, C.; Kranz, L.; Keller, D.; Gretener, C.; Hagendorfer, H.; Jaeger, D.; Erni, R.; Nishiwaki, S.; Buecheler, S.; Tiwari, A. N. Potassium-Induced Surface Modification of Cu(In,Ga)Se₂ Thin Films for High-Efficiency Solar Cells. *Nat. Mater.* **2013**, *12*, 1107−1111.

(11) First Solar. *First Solar Achieves Yet Another Cell Conversion Efficiency World Record.* Press Release, 2016.

(12) Yang, W. S.; Park, B.-W.; Jung, E. H.; Jeon, N. J.; Kim, Y. C.; Lee, D. U.; Shin, S. S.; Seo, J.; Kim, E. K.; Noh, J. H.; Seok, S. I. Iodide management in formamidinium-lead-halide-based perovskite layers for efficient solar cells. *Science* **2017**, *356*, 1376−1379.

(13) Sze, S. M. *Physics of Semiconductor Devices*; John Wiley & Sons, 1981.

(14) Beer, A. C. The Hall Effect and Related Phenomena. *Solid-State Electron.* **1966**, *9*, 339−351.

(15) Blood, P.; Orton, J. W. *The Electrical Characterization of Semiconductors: Majority Carriers and Electron States*; Academic Press: London, 1992.

(16) Schroder, D. K. *Semiconductor Material and Device Characterization*; John Wiley & Sons, 1990.

(17) Hegedus, S. S.; Shafarman, W. N. Thin-film Solar Cells: Device Measurements and Analysis. *Prog. Photovoltaics Res. Appl.* **2004**, *12*, 155−176.

(18) Sozzi, G.; Lazzarini, M.; Menozzi, R.; Carron, R.; Avancini, E.; Bissig, B.; Buecheler, S.; Tiwari, A. N. A Numerical Study of the Use of C-V Characteristics to Extract the Doping Density of CIGS Absorbers. *Proceedings of the 43rd IEEE Photovoltaic Specialists Conference*, 2016; pp 2283−2288.

(19) Werner, F. Hall Measurements on Low-Mobility Thin Films. *J. Appl. Phys.* **2017**, *122*, 135306.

(20) Lauwaert, J.; Lauwaert, J.; Van Puyvelde, L.; Thybaut, J. W.; Vrielinck, H. Modeling of Capacitance Transients of Thin-film Solar Cells: A Valuable Tool to Gain Information on Perturbing Layers or Interfaces. *Appl. Phys. Lett.* **2014**, *104*, 053502.

(21) Lauwaert, J.; Van Puyvelde, L.; Lauwaert, J.; Thybaut, J. W.; Khelifi, S.; Burgelman, M.; Pianezzi, F.; Tiwari, A. N.; Vrielinck, H. Assignment of Capacitance Spectroscopy Signals of CIGS Solar Cells to Effects of Non-ohmic Contacts. *Sol. Energy Mater. Sol. Cells* **2013**, *112*, 78−83.

(22) Sozzi, G.; Napoli, S. D.; Menozzi, R.; Werner, F.; Siebentritt, S.; Jackson, P.; Witte, W. Influence of Conduction Band Offsets at Window/Buffer and Buffer/Absorber Interfaces on the Roll-over of J-V Curves of CIGS Solar Cells. *Proceedings of the 44th IEEE Photovoltaic Specialists Conference*, 2017; p 628.

(23) Werner, F.; Siebentritt, S. Buffer Layers, Defects, and the Capacitance Step in the Admittance Spectrum of a Thin-Film Solar Cell. *Phys. Rev. Appl.* **2018**, *9*, 054047.

(24) Werner, F.; Zelenina, A.; Siebentritt, S. Experimental Evidence For CdS-related Transport Barrier in Thin Film Solar Cells and Its Impact on Admittance Spectroscopy. *Proceedings of the 44th IEEE Photovoltaic Specialists Conference*, 2017; p 709.

(25) Heath, J.; Zabierowski, P. Capacitance Spectroscopy of Thin-Film Solar Cells. *Advanced Characterization Techniques for Thin Film Solar Cells*, 2011.

(26) Eisenbarth, T.; Unold, T.; Caballero, R.; Kaufmann, C. A.; Schock, H.-W. Interpretation of admittance, capacitance-voltage, and current-voltage signatures in Cu(In,Ga)Se2 thin film solar cells. *J. Appl. Phys.* **2010**, *107*, 034509.

(27) Rau, U.; Braunger, D.; Herberholz, R.; Schock, H. W.; Guillemoles, J.-F.; Kronik, L.; Cahen, D. Oxygenation and air-annealing effects on the electronic properties of Cu(In,Ga)Se2 films and devices. *J. Appl. Phys.* **1999**, *86*, 497−505.

(28) Rau, U.; Schmidt, M. Electronic properties of ZnO/CdS/Cu(In,Ga)Se2 solar cells - aspects of heterojunction formation. *Thin Solid Films* **2001**, *387*, 141−146.

(29) Herberholz, R.; Igalson, M.; Schock, H. W. Distinction between bulk and interface states in CuInSe2/CdS/ZnO by space charge spectroscopy. *J. Appl. Phys.* **1998**, *83*, 318−325.

(30) Heath, J. T.; Cohen, J. D.; Shafarman, W. N. Bulk and metastable defects in CuIn1−xGaxSe2 thin films using drive-level capacitance profiling. *J. Appl. Phys.* **2004**, *95*, 1000−1010.

(31) Reislöhner, U.; Ronning, C. Maxwell-Wagner Polarization in Cu(In,Ga)(S,Se)₂. *Appl. Phys. Lett.* **2012**, *100*, 252111.

(32) Reislöhner, U.; Metzner, H.; Ronning, C. Hopping Conduction Observed in Thermal Admittance Spectroscopy. *Phys. Rev. Lett.* **2010**, *104*, 226403.

(33) Burgelman, M.; Nollet, P. Admittance Spectroscopy of Thin Film Solar Cells. *Solid State Ionics* **2005**, *176*, 2171−2175.

(34) Igalson, M.; Urbaniak, A.; Edoff, M. Reinterpretation of Defect Levels Derived From Capacitance Spectroscopy of CIGSe Solar Cells. *Thin Solid Films* **2009**, *517*, 2153−2157.

(35) Lauwaert, J.; Callens, L.; Khelifi, S.; Decock, K.; Burgelman, M.; Chirila, A.; Pianezzi, F.; Buecheler, S.; Tiwari, A. N.; Vrielinck, H. About RC-like contacts in deep level transient spectroscopy and Cu(In,Ga)Se2 solar cells. *Prog. Photovoltaics Res. Appl.* **2012**, *20*, 588−594.

(36) Werner, F.; Wolter, M. H.; Siebentritt, S.; Sozzi, G.; Napoli, S. D.; Menozzi, R.; Jackson, P.; Witte, W.; Carron, R.; Avancini, E.; Weiss, T. P.; Buecheler, S. Alkali Treatments of Cu(In,Ga)Se₂ Thin-Film Absorbers and Their Impact on Transport Barriers. *Prog. Photovoltaics Res. Appl.* **2018**, 3032.

(37) Christoforou, N.; Leslie, J. D.; Damaskinos, S. Current-voltage, capacitance-voltage, and capacitance-temperature measurements on CdS/CuInSe2 solar cells. *Sol. Cells* **1989**, *26*, 215−225.

(38) Ćwil, M.; Igalson, M.; Zabierowski, P.; Kaufmann, C. A.; Neisser, A. Capacitance Profiling in the CIGS Solar Cells. *Thin Solid Films* **2007**, *515*, 6229−6232.

(39) Cwil, M.; Igalson, M.; Zabierowski, P.; Siebentritt, S. Charge and doping distributions by capacitance profiling in Cu(In,Ga)Se2 solar cells. *J. Appl. Phys.* **2008**, *103*, 063701.

(40) Werner, F.; Bertram, T.; Mengozzi, J.; Siebentritt, S. What is the dopant concentration in polycrystalline thin-film Cu(In,Ga)Se 2 ? *Thin Solid Films* **2017**, *633*, 222−226.

(41) Abou-Ras, D.; Kostorz, G.; Romeo, A.; Rudmann, D.; Tiwari, A. N. Structural and chemical investigations of CBD- and PVD-CdS buffer layers and interfaces in Cu(In,Ga)Se2-based thin film solar cells. *Thin Solid Films* **2005**, *480−481*, 118−123.

(42) Liao, D.; Rockett, A. Cd doping at the CuInSe2/CdS heterojunction. *J. Appl. Phys.* **2003**, *93*, 9380−9382.

(43) Nakada, T.; Kunioka, A. Direct evidence of Cd diffusion into Cu(In, Ga)Se2 thin films during chemical-bath deposition process of CdS films. *Appl. Phys. Lett.* **1999**, *74*, 2444−2446.

(44) Ramanathan, K.; Noufi, R.; Granata, J.; Webb, J.; Keane, J. Prospects for in situ junction formation in CuInSe2 based solar cells. *Sol. Energy Mater. Sol. Cells* **1998**, *55*, 15−22.

(45) Ümsür, B.; Calvet, W.; Höpfner, B.; Steigert, A.; Lauermann, I.; Gorgoi, M.; Prietzel, K.; Navirian, H. A.; Kaufmann, C. A.; Unold, T.; Lux-Steiner, M. C. Investigation of Cu-poor and Cu-rich Cu(In,Ga)Se 2 /CdS interfaces using hard X-ray photoelectron spectroscopy. *Thin Solid Films* **2015**, *582*, 366−370.

(46) Bekaert, J.; Saniz, R.; Partoens, B.; Lamoen, D. Native point defects in CuIn1−xGaxSe2: hybrid density functional calculations predict the origin of p- and n-type conductivity. *Phys. Chem. Chem. Phys.* **2014**, *16*, 22299−22308.

(47) Oikkonen, L. E.; Ganchenkova, M. G.; Seitsonen, A. P.; Nieminen, R. M. Formation, migration, and clustering of point defects in CuInSe2from first principles. *J. Phys.: Condens. Matter* **2014**, *26*, 345501.

(48) Pohl, J.; Albe, K. Intrinsic Point Defects in CuInSe$_2$ and CuGaSe$_2$ As Seen Via Screened-Exchange Hybrid Density Functional Theory. *Phys. Rev. B: Condens. Matter Mater. Phys.* **2013**, *87*, 245203.

(49) Werner, F.; Colombara, D.; Melchiorre, M.; Valle, N.; El Adib, B.; Spindler, C.; Siebentritt, S. Doping mechanism in pure CuInSe2. *J. Appl. Phys.* **2016**, *119*, 173103.

(50) Maeda, T.; Wada, T. First-Principles Studies on Cd Doping in CuInSe2and Related Compounds during Chemical Bath Deposition of CdS Buffer Layer. *Jpn. J. Appl. Phys.* **2013**, *52*, 061201.

(51) Persson, C.; Zhao, Y.-J.; Lany, S.; Zunger, A. N-Type Doping of CuInSe$_2$ and CuGaSe$_2$. *Phys. Rev. B: Condens. Matter Mater. Phys.* **2005**, *72*, 035211.

(52) Varley, J. B.; Lordi, V. Intermixing at the Absorber-Buffer Layer Interface in Thin-Film Solar Cells: The Electronic Effects of Point Defects in Cu(In,Ga)(Se,S)2 and Cu2ZnSn(Se,S)4 Devices. *J. Appl. Phys.* **2014**, *116*, 063505.

(53) Abe, T.; Kashiwaba, Y.; Baba, M.; Imai, J.; Sasaki, H. XPS Analysis of P-Type Cu-Doped CdS Thin Films. *Appl. Surf. Sci.* **2001**, *175–176*, 549−554.

(54) Buffière, M.; Gautron, E.; Hildebrandt, T.; Harel, S.; Guillot-Deudon, C.; Arzel, L.; Naghavi, N.; Barreau, N.; Kessler, J. Composition and structural study of solution-processed Zn(S,O,OH) thin films grown using H2O2 based deposition route. *Thin Solid Films* **2013**, *535*, 171−174.

(55) Hubert, C.; Naghavi, N.; Roussel, O.; Etcheberry, A.; Hariskos, D.; Menner, R.; Powalla, M.; Kerrec, O.; Lincot, D. The Zn(S,O,OH)/ZnMgO buffer in thin film Cu(In,Ga)(S,Se)2-based solar cells part I: Fast chemical bath deposition of Zn(S,O,OH) buffer layers for industrial application on Co-evaporated Cu(In,Ga)Se2and electrodeposited CuIn(S,Se)2solar cells. *Prog. Photovoltaics Res. Appl.* **2009**, *17*, 470−478.

(56) Regesch, D.; Gütay, L.; Larsen, J. K.; Deprédurand, V.; Tanaka, D.; Aida, Y.; Siebentritt, S. Degradation and passivation of CuInSe2. *Appl. Phys. Lett.* **2012**, *101*, 112108.

(57) Weiss, T. P.; Redinger, A.; Regesch, D.; Mousel, M.; Siebentritt, S. Direct Evaluation of Defect Distributions From Admittance Spectroscopy. *IEEE J. Photovolt.* **2014**, *4*, 1665−1670.

(58) Pudov, A. O.; Sites, J. R.; Contreras, M. A.; Nakada, T.; Schock, H.-W. CIGS J-V Distortion in the Absence of Blue Photons. *Thin Solid Films* **2005**, *480–481*, 273−278.

(59) van Opdorp, C. Evaluation of Doping Profiles From Capacitance Measurements. *Solid-State Electron.* **1968**, *11*, 397−406.

(60) Bastek, J.; Stolwijk, N. A.; Wuerz, R.; Eicke, A.; Albert, J.; Sadewasser, S. Zinc diffusion in polycrystalline Cu(In,Ga)Se2 and single-crystal CuInSe2 layers. *Appl. Phys. Lett.* **2012**, *101*, 074105.

(61) Hiepko, K.; Bastek, J.; Schlesiger, R.; Schmitz, G.; Wuerz, R.; Stolwijk, N. A. Diffusion and incorporation of Cd in solar-grade Cu(In,Ga)Se2 layers. *Appl. Phys. Lett.* **2011**, *99*, 234101.

(62) Kazmerski, L. L. Grain Boundary and Interdiffusion Studies in Compound Semiconductor Thin Films and Devices Utilizing Auger Electron Spectroscopy and Secondary Ion Mass Spectroscopy. *Thin Solid Films* **1979**, *57*, 99−106.

(63) Nakada, T. Nano-structural investigations on Cd-doping into Cu(In,Ga)Se 2 thin films by chemical bath deposition process. *Thin Solid Films* **2000**, *361–362*, 346−352.

(64) Rusu, M.; Bär, M.; Lehmann, S.; Sadewasser, S.; Weinhardt, L.; Kaufmann, C. A.; Strub, E.; Röhrich, J.; Bohne, W.; Lauermann, I.; Jung, C.; Heske, C.; Lux-Steiner, M. C. Three-dimensional structure of the buffer/absorber interface in CdS/CuGaSe2 based thin film solar cells. *Appl. Phys. Lett.* **2009**, *95*, 173502.

(65) Nishimura, T.; Toki, S.; Sugiura, H.; Nakada, K.; Yamada, A. Effect of Cu-deficient layer formation in Cu(In,Ga)Se2 solar-cell performance. *Prog. Photovoltaics Res. Appl.* **2018**, *26*, 291−302.

(66) Abou-Ras, D.; Schäfer, N.; Hages, C. J.; Levcenko, S.; Márquez, J.; Unold, T. Inhomogeneities in Cu(In,Ga)Se2 Thin Films for Solar Cells: Band-Gap Versus Potential Fluctuations. *Sol. RRL* **2018**, *2*, 1700199.

(67) Krause, M.; Nikolaeva, A.; Marquez, J.; Hages, C.; Levcenko, S.; Unold, T.; Witte, W.; Hariskos, D.; Abou-Ras, D. *Insight into Local Fluctuations of Net Doping and Lifetime in Cu(In,Ga)Se2 Solar Cells, Presented at DPG Spring Meeting Berlin, Germany*, 2018.

(68) Bauknecht, A.; Siebentritt, S.; Albert, J.; Lux-Steiner, M. C. Radiative recombination via intrinsic defects in CuxGaySe2. *J. Appl. Phys.* **2001**, *89*, 4391−4400.

(69) Siebentritt, S.; Rega, N.; Zajogin, A.; Lux-Steiner, M. C. Do we really need another PL study of CuInSe2? *Phys. Status Solidi C* **2004**, *1*, 2304−2310.

(70) Schuler, S.; Siebentritt, S.; Nishiwaki, S.; Rega, N.; Beckmann, J.; Brehme, S.; Lux-Steiner, M. C. Self-Compensation of Intrinsic Defects in the Ternary Semiconductor CuGaSe$_2$. *Phys. Rev. B: Condens. Matter Mater. Phys.* **2004**, *69*, 045210.

(71) Unold, T.; Gütay, L. Photoluminescence Analysis of Thin-Film Solar Cells. *Advanced Characterization Techniques for Thin Film Solar Cells*, 2011.

(72) Babbe, F.; Choubrac, L.; Siebentritt, S. Quasi Fermi level splitting of Cu-rich and Cu-poor Cu(In,Ga)Se2 absorber layers. *Appl. Phys. Lett.* **2016**, *109*, 082105.